Critical states and anomalous mobility edges in two-dimensional diagonal quasicrystals

Callum W. Duncan *

Department of Physics and SUPA, University of Strathclyde, Glasgow G4 0NG, United Kingdom

(Received 20 October 2023; revised 16 December 2023; accepted 28 December 2023; published 16 January 2024)

We study the single-particle properties of two-dimensional quasicrystals where the underlying geometry of the tight-binding lattice is crystalline but the on-site potential is quasicrystalline. We will focus on the two-dimensional (2D) generalized Aubry-André model which has a varying form to its quasiperiodic potential, through a deformation parameter and varied irrational periods of cosine terms, which allows a continuous family of on-site quasicrystalline models to be studied. We show that the 2D generalized Aubry-André model exhibits many single-particle mobility edges which we confirm for finite systems and supports critical states across large parameter regions. Critical states are neither fully localized nor extended. We observe that diagonal quasicrystalline models can support many energy intervals of critical states in the spectrum while stabilizing both localized and extended states in other energy intervals; we refer to these as anomalous mobility edges. We show that critical states are present independent of system size through a scaling analysis of the inverse participation ratio and that they are present in spectra that also contain extended and localized states, confirming that at least one anomalous mobility edge is present. Due to this, these models exhibit anomalous diffusion of initially localized states across the majority of parameter regions, including deep in the normally localized regime. The presence of critical states in large parameter regimes and throughout the spectrum will have consequences for the many-body properties of quasicrystals, including the formation of the Bose glass and the potential to host a many-body localized phase.

DOI: 10.1103/PhysRevB.109.014210

I. INTRODUCTION

Quasicrystalline systems are an intriguing intermediary between periodic crystalline and amorphous disordered systems [1–3], characterized by the presence of long-range order and short-range disorder. There has been extensive study of their electronic properties by considering one-dimensional quasiperiodic models including interactions [4,5], where the quasiperiodic nature of the system is included within the parameters and vertex models of aperiodic tilings [6–9], which largely probe the physics due to their quasicrystalline geometry. One of the most intriguing properties of quasicrystals is their potential to host a many-body localized phase in two dimensions (2D), due to the conjecture that there is an absence of rare regions [10–14].

The physical properties of many-body quasicrystalline systems is an open question, especially beyond one dimension, due to the complexity of theoretically simulating two-dimensional many-body systems. The quasicrystalline nature of the system often leads to the presence of frustration due to short-range disorder, while long-range order means that large system sizes are required to probe physical properties. This is potentially an area where quantum simulators with cold atoms, as have been pursued for 2D quasicrystals [15–18], could have a significant impact. This has inspired a number of recent works both looking at Hubbard-type lattice models [19–23] and looking at continuous quantum Monte Carlo methods [24–26] for ultracold atoms in optical quasicrystalline lattices. However, in order to fully understand the physical interplay of quasiperiodicity and interactions, we first need to further develop our understanding of single-particle quasicrystalline models in 2D.

A typical example of a tight-binding quasicrystal is the one-dimensional Aubry-André (AA) model, which has a transition between extended and localized states and is described by the sampling of a cosine term of irrational period with the spacing of a tight-binding model [27–29]. It is known that the one-dimensional AA model does not have a mobility edge but modified versions of the AA model can exhibit mobility edges. An example of this is the 1D generalized AA (GAA) model, which exhibits a mobility edge and a mixed intermediary regime between extended and localized states in a related family of quasiperiodic potentials by introducing a deformation of the AA potential [30–37]; we will introduce this model in detail in Sec. II A. Recently, the 1D GAA model has been explored in experimental realizations utilizing ultracold atoms [38,39] which included the interplay of interactions and quasicrystalline order. A related realization of the 1D AA model was also recently studied using cavity polaritons [40]; in this case the experimental potential was mapped between the AA and Fibonacci chains to explore a family of quasicrystalline models.

*callum.duncan@strath.ac.uk

An interesting property of quasicrystals is that they can host critical states away from transition regions. Critical states are characterized by being neither fully localized nor extended in the space that supports them and are multifractal in the Hilbert space. When moving to two-dimensional models, the role of critical states becomes important. This has been well studied in vertex models of quasicrystals [41–45], which are quasiperiodic through a variation of the local coordination number with the on-site term normally set to zero. It is known that two-dimensional generalizations of the AA model can host partially extended states, which are critical states, due to weak modulation lines in the potential [46]. Weak modulation refers to a relatively low disorder in regions of the potential in comparison to the strength of the quasiperiodic potential. Note that it does not mean that the potential itself is weak in this region, but that the disorder is relatively low across the region. It has also recently been observed that some one-dimensional quasicrystals can exhibit so-called anomalous mobility edges between energy intervals of localized and critical states in the spectrum [47–49]. The main motivation of this work is to extend upon these prior observations and build a picture of the single-particle behavior of 2D quasicrystalline models, where the quasiperiodic term is from the on-site component of a tight-binding Hamiltonian, with a particular focus on the role of critical states. While we will focus on the single-particle picture, some of the impact of the critical states in the many-body regime has already been probed by the consideration of superfluid and transport properties that are supported by the weak modulation of the potential in certain regions [21,22,50].

In this paper we will first define the 2D GAA model and the measures that will be utilized to distinguish localized, extended, and critical states. We will then show in Sec. III that the 2D GAA model exhibits many mobility edges instead of a single mobility edge and an intermediate regime between localized and extended states. We next show in Sec. III D that the presence of many mobility edges and critical states is not unique to our choice of parameters in the 2D GAA model, with an example of a bichromatic potential. We then consider a few example cases to study the presence of mobility edges in the spectrum and show that there are anomalous mobility edges in the 2D GAA model between both localized and critical states and extended and critical states. In Sec. IV B, we consider the impact of the presence of critical states and mobility edges on the dynamical properties of initially localized states. Finally, we summarize our findings and key open questions in Sec. V.

II. THE 2D GENERALIZED AUBRY-ANDRÉ MODEL AND PROPERTIES

A. Model

We consider the single-particle physics of a family of 2D on-site quasiperiodic tight-binding models given by the Hamiltonian

$$H = -J \sum_{\langle i,j \rangle} (\hat{b}_i^\dagger \hat{b}_j + \text{H.c.}) - \lambda \sum_i V_\beta(i) \hat{n}_i, \tag{1}$$

with tunneling coefficient J, on-site modulation strength λ, on-site potential deformation parameter β, $\hat{b}_i^\dagger$ ($\hat{b}_i$) being the creation (annihilation) operator of a particle at the ith site, $\hat{n}_i$ being the number operator, and $\langle i, j \rangle$ denoting nearest neighbors. We define the state of the system $|\Psi\rangle$ as

$$|\Psi\rangle = \sum_i \psi(x_i, y_i)|i\rangle, \tag{2}$$

where $|i\rangle$ labels the state with a single particle occupying the site labeled by (x_i, y_i) with $\psi(x_i, y_i)$ being the coefficients that fully define the single-particle state, and which we will refer to as the wave function or state. We will consider the geometry of the lattice to be a standard 2D square lattice, though the general results do not rely on this choice of geometry.

We will consider the family of quasiperiodic models defined by an extension of the 1D GAA model [30] to 2D giving an on-site potential of

$$V_\beta(i) = \frac{V_{\text{AA}}(x_i, y_i)}{1 - \beta V_{\text{AA}}(x_i, y_i)}, \tag{3}$$

with the 2D AA potential being

$$V_{\text{AA}}(x_i, y_i) = \cos(2\pi(x_i + y_i)/\tau_1) + \cos(2\pi(x_i - y_i)/\tau_2). \tag{4}$$

Moving forward, we will drop the i label for each site and simply label sites via their (x, y) coordinates in the lattice. By varying $\beta \in (-0.5, 0.5)$ in Eq. (3), a family of quasiperiodic potentials is explored as long as the periods τ_1 and τ_2 are irrational. We will consider an $L \times L$ lattice with open boundary conditions and by default take $\tau_1 = \tau_2 = \sqrt{2}$ with other irrational τ expected to explore similar physics. We will consider lattices of length $L = 60$ sites unless otherwise stated. The 2D AA model is given at $\beta = 0$ and is self-dual at $\lambda = 2J$ as is shown in the Appendix of Ref. [46]. However, the states do not all localize at the self-dual point, as is the case for the 1D AA model, due to the two-dimensional nature of this model. The 2D GAA potential contains divergences for $\beta = \pm 0.5$, which we will not consider or closely approach, with the largest we will consider being $\beta = 0.4$. Note that it is also possible to couple different one-dimensional chains of the AA potential in order to build a 2D generalization of the AA model [51]. This approach of "stacking" AA chains can be considered both with and without quasicrystalline order in the stacking dimension, with the results presented here expected to be similar to those of stacking AA chains with each chain being deformed according to a quasiperiodic distribution.

Examples of the 2D GAA model for $\tau_1 = \tau_2$ and an example for $\tau_1 \neq \tau_2$ are shown in Fig. 1. In the case of $\tau_1 = \tau_2$ in Figs. 1(a)–1(c), weak modulation lines can be clearly observed, where the potential varies little across a line through the lattice. We also observe that in the case of $\tau_1 \neq \tau_2$ in Fig. 1(d) there are still weak modulation regions that percolate through the lattice. However, when the symmetry of $\tau_1 = \tau_2$ is removed, the weak modulation does not appear along lines which match the geometry of the underlying square lattice. We will show that critical states rely on the presence of these weak modulation regions but do not fundamentally require these regions to appear in the form of lines along the square lattice. An approximate condition for weak modulation to occur can be found by considering $V_\beta(i) \approx 0$. For $\tau_1 = \tau_2$, $V_\beta(i) \approx 0$ is met for

$$x - \frac{k}{4\tau} \approx 0$$

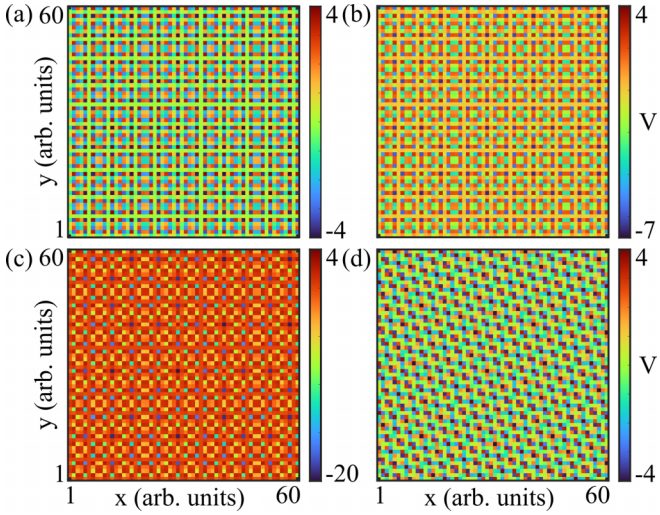

FIG. 1. The potential of the 2D GAA model on a square lattice for $\lambda/J = 2$. The case of equal irrational periods of $\tau_1 = \tau_2 = \sqrt{2}$ with a deformation of (a) $\beta = 0$, (b) $\beta = 0.2$, and (c) $\beta = 0.4$. The case of unequal irrational periods of $\tau_1 = \sqrt{2}$ and $\tau_2 = (1+\sqrt{5})/2$ is shown in (d) with a deformation of $\beta = 0$.

and

$$y - \frac{k}{4\tau} \approx 0,$$

with k being an odd integer [22]. For $\tau_1 \neq \tau_2$, approximate conditions can also be derived; however, these are rather more complicated and are not separate in x and y, which is why weak modulation does not occur along lines in this case, an example of which is shown in Fig. 1(d).

We briefly note that the 2D GAA model can be implemented in current cold atom setups in a similar way to the 1D GAA model [32], i.e., by considering the limit of $\beta \ll 1$ as expanding $V_\beta(x, y)$ around $\beta = 0$ gives

$$V_\beta(x, y) \approx V_{\mathrm{AA}}(x, y) + \beta[V_{\mathrm{AA}}(x, y)]^2 + O(\beta^2). \tag{5}$$

The additional term proportional to β can be realized through the introduction of an additional lattice field along the direction of the square lattice and the AA modulation. There have also been proposals to realize the 1D GAA model via photonic lattices [52], and the 2D GAA model could be considered in a similar setting.

B. Participation ratios

The inverse participation ratio is a measure of the localization of a quantum state within its Hilbert space. We will consider the inverse participation ratio,

$$\mathrm{IPR}_n = \sum_{x,y} |\psi(x, y)|^4, \tag{6}$$

and the normalized participation ratio,

$$\mathrm{NPR}_n = \left(L^2 \sum_{x,y} |\psi(x, y)|^4 \right)^{-1}, \tag{7}$$

of each state. We will also average over all states to gain an insight into the overall behavior of the system, and we will denote this by $\langle \mathrm{IPR} \rangle$ and $\langle \mathrm{NPR} \rangle$, with $\langle \cdot \rangle$ denoting the average over all states. We can utilize the participation ratios to qualitatively determine how localized the states are within the Hilbert space, with localized states defined by $\langle \mathrm{IPR} \rangle \sim O(1)$ and $\langle \mathrm{NPR} \rangle \sim 0$ and extended states defined by $\langle \mathrm{IPR} \rangle \sim 0$ and $\langle \mathrm{NPR} \rangle \sim O(1)$. A third intermediate regime where the spectrum is partially localized or extended can be defined when both $\langle \mathrm{IPR} \rangle \sim O(1)$ and $\langle \mathrm{NPR} \rangle \sim O(1)$. Note that this intermediate regime does not immediately imply the presence of critical states and will occur when you have a mobility edge between localized and extended states in the spectrum. The average IPR and NPR also only give a qualitative picture of the localization of the states with the numerical values being sensitive to the finite size of the system. We will consider this dependence on system size in more detail in Sec. III C, including a scaling analysis.

C. Fractal dimensions

Multifractal analysis of the wave function can distinguish between critical, localized, and extended states. This has been useful in characterizing the states at the metal-insulator transition of Anderson localization [53–57], one-dimensional quasiperiodic models [58–61], and two-dimensional quasiperiodic tilings [62,63].

To calculate a system's fractal dimensions, we first split the probability density into N_l boxes of linear size l with the system being of linear size L and d dimensional. The probability of finding the particle in the kth box is given by

$$\mu_k(l) = \sum_{i \in l^d} |\psi(x_i, y_i)|^2, \tag{8}$$

where i runs over all sites within the box. The qth moment of the probability measure is

$$P_q(l) = \sum_{k=1}^{N_l} \mu_k^q(l). \tag{9}$$

Within a certain range of the box scaling $\kappa = l/L$ the moments will show a power-law scaling with an exponent $\eta(q)$, that is,

$$P_q(\kappa) \propto (\kappa)^{\eta(q)}. \tag{10}$$

This exponent (often called the mass exponent) is defined as

$$\eta(q) = \begin{cases} d(q-1) & \text{extended} \\ 0 & \text{localized} \\ D_q(q-1) & \text{critical,} \end{cases} \tag{11}$$

where d is the physical space dimension. For a critical state, the exponent is dependent on the fractal dimension D_q.

We will utilize the fractal dimension to characterize the critical states of the 2D GAA model by focusing on measuring the $q = 2$ fractal dimension, as this is equivalent to the box-counting dimension often used for fractal structures and measures the spread of the wave function over the supporting Hilbert space. In this case, the Hilbert space is the physical lattice, meaning that D_2 is a measure of locality in space, with

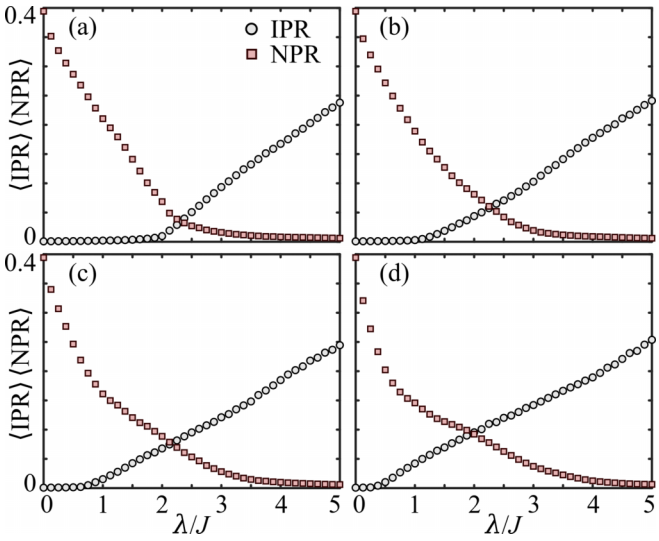

FIG. 2. The mean over all states of the inverse and normalized participation ratios for the 2D GAA model. Shown are the cases of (a) $\beta = 0$ (the 2D Aubry-André model), (b) $\beta = 0.2$, (c) $\beta = 0.3$, and (d) $\beta = 0.4$. The intermediate regime, where both $\langle \text{IPR} \rangle$ and $\langle \text{NPR} \rangle$ are larger than zero, is shown to grow with increasing β.

$D_2 = 0$ for localized states, $D_2 = d$ for extended states, and $0 < D_2 < d$ for critical states.

III. LOCALIZATION, MOBILITY EDGES, AND CRITICAL STATES

A. The intermediate regime

We will now consider the localization properties of the 2D GAA model. It has been shown that the 1D GAA and other 1D quasiperiodic models have an intermediate regime where localized and extended states coexist [34]. In 1D, this intermediate regime is related to the presence of at least one mobility edge in the spectrum between localized and extended states and is identified by both the mean inverse and normalized participation ratios being nonzero.

It is known that the 2D Aubry-André model (the case of $\beta = 0$) is self-dual [46] and that this occurs at $\lambda = 2J$. The model then has mostly extended states for $\lambda < 2J$, localized states for $\lambda > 2J$, and critical states at the transition point $\lambda = 2J$. However, it was observed recently that this model also exhibits states that are partially extended, i.e., critical, over a large range of λ away from the transition at $\lambda = 2J$ [46]. However, the presence of partially extended or critical states does not guarantee that there is a mobility edge between localized and extended states or that there is a mix of localized and extended states at any given λ.

We observe in Fig. 2(a) that the 2D AA model has only a small region $\lambda > 2J$ (the self-dual point [46]) where there is both a finite $\langle \text{IPR} \rangle$ and a finite $\langle \text{NPR} \rangle$ and there is unlikely to be a significant mobility edge across a range of λ between localized and extended states. As we increase the deformation parameter β in Figs. 2(b)–2(d) we observe a broadening of the intermediate regime. This eventually reaches a point where the intermediate regime extends across a large range of modulation strengths for $\beta \geqslant 0.3$, as seen in Figs. 2(c) and 2(d). With

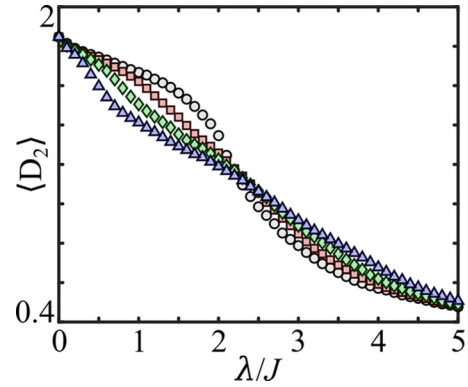

FIG. 3. The mean scaling fractal dimension, D_2, of the 2D GAA model. Shown are the cases of $\beta = 0$ (gray circles), $\beta = 0.2$ (red squares), $\beta = 0.3$ (green diamonds), and $\beta = 0.4$ (blue triangles). There is no clear signature of the intermediate regime changing in size as a function of λ, and the different quasiperiodic models show little difference in mean D_2.

such a large region of mixed localized and extended states, it is expected that the system will contain at least one mobility edge that is being tuned with the deformation of the potential and stable with respect to λ. The 1D GAA model exhibits a similar tuning of the intermediate regime with β.

We also consider in Fig. 3 the mean scaling fractal dimension given by $\langle D_2 \rangle$ for a range of deformations β. If the majority of the states are either localized or extended, then we would expect to see a clear transition in the mean fractal dimension. Then as we tune the modulation β we would expect the transition to be "smoothed" due to the presence of a mix of extended and localized states with a corresponding mobility edge. We do observe in Fig. 3 the expected smoothing of the transition in $\langle D_2 \rangle$ due to the presence of at least one mobility edge as β increases. However, we note that the transition in $\langle D_2 \rangle$ is already rather smooth and not sharp for the 2D AA model but this model has been shown to have only a small intermediate regime in Fig. 2(a). The smoothing of the transition in $\langle D_2 \rangle$ with increasing deformation β is also relatively minor compared with the large intermediate regions observed in Figs. 2(b)–2(d). The fact that there are narrow and broad intermediate regimes but always a relatively smooth interpolation in $\langle D_2 \rangle$ may appear contradictory, but the reasons behind this apparent discrepancy will become clear as we consider the critical states that are present in Sec. III C.

B. Mobility edges

We have shown that there exists a third intermediate mixed regime between localized and extended states for the 2D GAA model. The presence of such a regime has normally been expected to reflect a mixture of localized and extended states in the spectrum and, hence, the presence of at least one mobility edge. We investigate the presence of mobility edges in the system by considering the individual NPR_n of each individual nth energy ordered state for a range of β and across the localization transition in λ, as is shown for four cases in Fig. 4. Note that similar results are obtained when considering the inverse participation ratio. First, we observe that the 2D

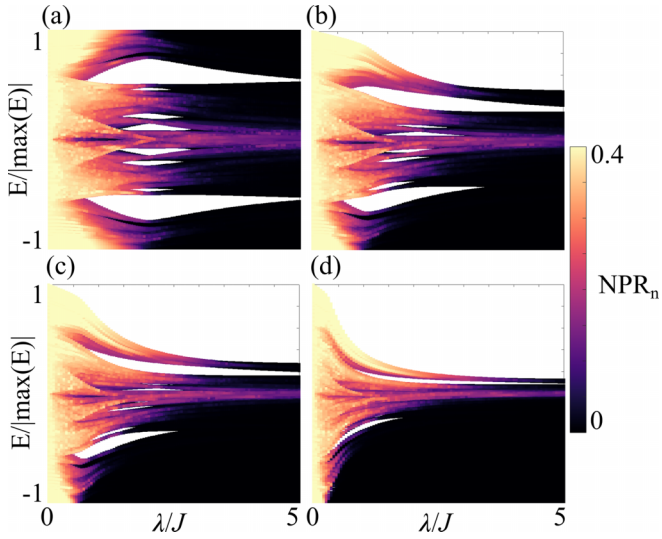

FIG. 4. The NPR of all states for the 2D GAA model as a function of the potential strength λ. Shown are the cases for a deformation of the potential of (a) $\beta = 0$, (b) $\beta = 0.2$, (c) $\beta = 0.3$, and (d) $\beta = 0.4$. The deformation of the potential allows for the formation of at least one mobility edge between localized and extended states in the spectrum for some λ.

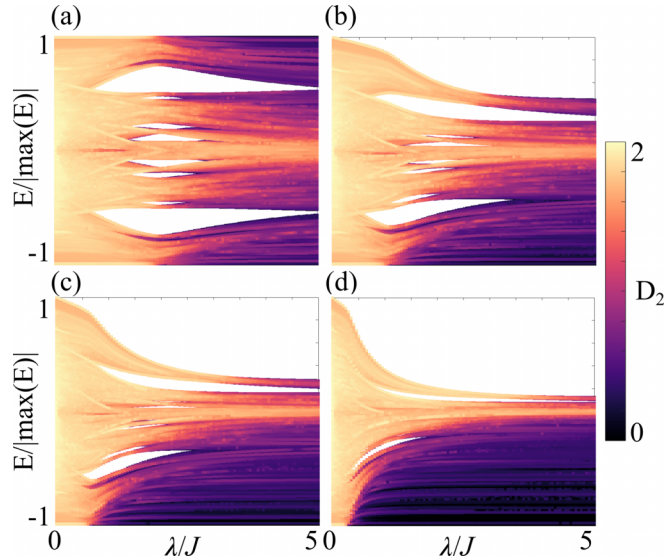

FIG. 5. Same as Fig. 4 but for the fractal scaling dimension D_2.

AA model ($\beta = 0$) has no clear single-particle mobility edge between localized and extended states, with the majority of states NPR $\to 0$ as we approach $\lambda/J = 2$. As we turn on the deformation, we observe that single-particle mobility edges are introduced, as shown in Figs. 4(b)–4(c) with NPR $\to 0$ faster for lower energy states.

However, in all cases of β in Fig. 4 there appear to be some moderately extended states with a finite NPR_n for even large λ centered around $E \sim 0$. These states are considerably localized in the 2D system, with NPR_n being not only small compared with the values in the extended regime but also noticeably resistant to converging to $\text{NPR}_n = 0$ as would be expected for a localized state far into the localized regime. We propose that what is being observed in the normalized participation ratio for large λ is in part the presence of critical states in the system with intermediate NPR as well as extended states. However, the normalized participation ratio alone is not sufficient to confirm this; therefore we consider in Fig. 5 the scaling fractal dimension D_2 of each state again in energy ordering and across the extended-to-localized transition in λ for the same β as in Fig. 4. With this we observe in all scenarios the presence of states with D_2 being consistent with the state being critical, i.e., neither $D_2 \to d$ nor $D_2 \to 0$. We note that finite-size effects impact the ideal convergence of D_2, and we have checked for individual states that it converges with increasing system size to d and 0 for extended and localized states, respectively. We will also discuss a scaling analysis of the IPR in Sec. III C which confirms that the critical states observed are present across a set of large systems. We note also that for some λ that would be expected to be in the localized regime, critical states dominate the central portion of the spectrum. Such regions could be expected to effectively remain in the extended or thermalizing phase, as the presence of many critical states will support the delocalization of a quantum state through the system; we will investigate this further in Sec. IV.

C. Critical states

We will briefly consider some examples of critical states on both sides of the localization transition. From the previous consideration of the scaling fractal dimension D_2, it can be seen that there are many states with intermediate D_2. Starting with the extended side of the localization transition, we consider the case of $\lambda/J = 1$. In the considered 60×60 system, there are far too many states to consider all of them, and we focus on two typical examples from each side of the transition. We first show a typical extended state in Fig. 6(a) with its corresponding fractal dimensions in Fig. 6(e). From inspection, the state is homogeneous and extended throughout the lattice. The fractal dimensions are also all $D_q \sim 2$, with deviations coming from the finite size of the system. A typical critical state for $\lambda < 2J$ is shown in Fig. 6(b) with its corresponding fractal dimensions in Fig. 6(f). The fractal dimensions make the nature of this state clear, with it varying across the moments q, which is a signature of a critical state.

Moving to the localized side of the transition, we consider the case of $\lambda/J = 4$. First, we show a typical localized state in Fig. 6(c); this is heavily localized, and its corresponding fractal dimensions tend to zero for positive moments and effectively a numerical infinity ($\gg 2$) for negative moments as shown in Fig. 6(g). A typical critical state on the localized side of the transition is shown in Fig. 6(d), and it has a far more clear multifractal nature than that for the extended regime. There are regions of the state that are extended along some directions and localized along others. When looking at the fractal dimension for this critical state in Fig. 6(h), it is large for negative q and is nonzero but small for positive q; this reflects the localized but extended nature of this critical state.

We now want to ensure that the observed critical states are not a finite-size effect and will probe the scaling of the mean IPR of all states within specific small energy windows

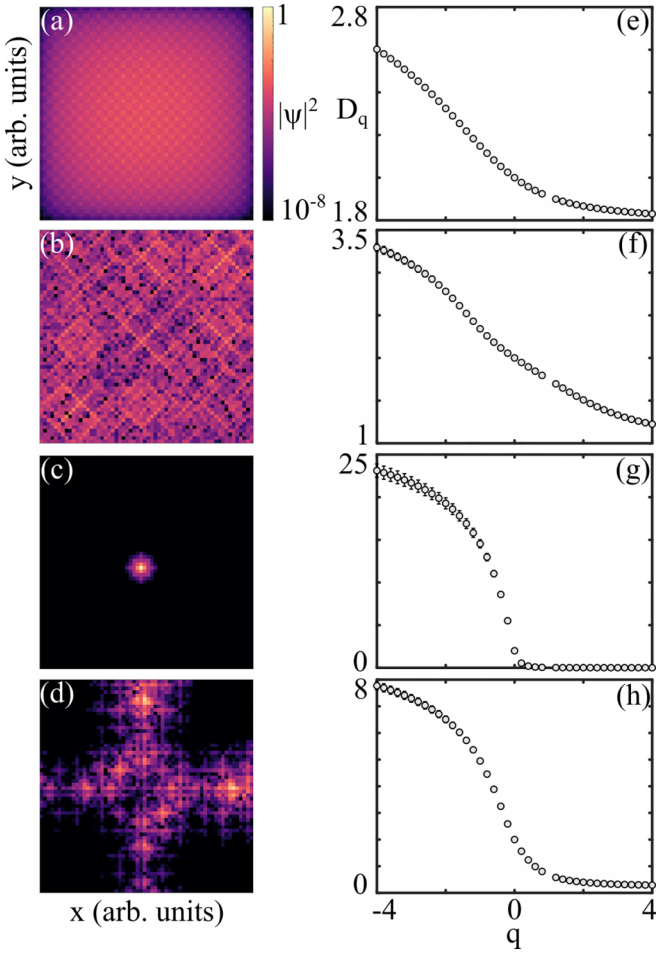

FIG. 6. Examples of localized and extended states and critical states [(a) and (b)] on both sides of the localization transition. We also plot the fractal dimensions [(e)–(h)] of the qth moment. On the extended side of the transition we consider (a) and (e) an extended state and (b) and (f) a critical state. On the localized side of the transition we consider (c) and (g) a localized state and (d) and (h) a critical state.

for increasing system size. The expected value of the IPR will scale with system size as IPR $\sim L^{\gamma}$, with $\gamma = 0$ for localized states, $\gamma = -d$ for extended states, and intermediate values being a signature of critical states [59]. We show examples of the scaling of the IPR for various energy windows for both the extended $\lambda = J$ and localized $\lambda = 3J$ regimes in Fig. 7 by varying the system size from 10^2 to 10^3 sites. This includes clear examples of critical states for the extended regime in Fig. 7(c), with $\gamma = -0.71 \pm 0.12$ in the energy window of $E/|\max(E)| \in [-0.0571, -0.0548]$, and the localized regime in Fig. 7(f), with $\gamma = -0.58 \pm 0.09$ in the energy window of $E/|\max(E)| \in [-0.1542, -0.1527]$. We have also confirmed that at least one anomalous mobility edge must exist independent of system size as this scaling analysis confirms that critical states exist in the same spectrum as localized states for $\lambda = 3J$ and extended states for $\lambda = J$.

To confirm that the scaling analysis above is probing the properties of similar states in a small energy window, and not the average of a large variation in IPR, we plot the variance of the IPR in the given energy windows in Fig. 8. From Fig. 8, we

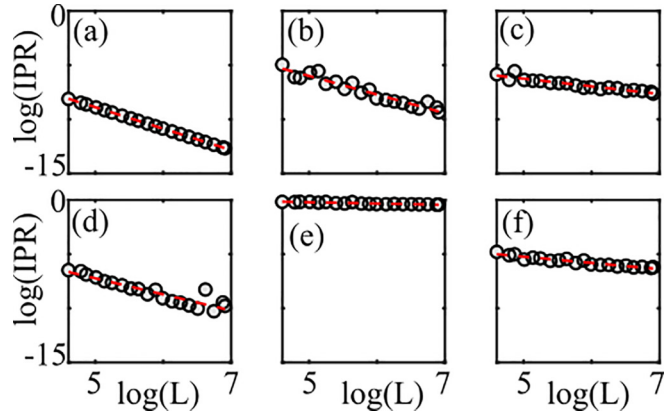

FIG. 7. Scaling of the mean IPR over all states within different energy windows for (a)–(c) $\lambda = J$ and (d)–(f) $\lambda = 3J$ for systems of linear size between $L = 100$ ($\log 100 = 4.6$) and 1000 ($\log 1000 = 6.9$). Linear fits to obtain γ are shown by a dashed red line in each plot. Energy windows are as follows: (a) $\bar{E} = E/|\max(E)| \in [-1, -0.9976]$ with $\gamma = -1.98 \pm 0.004$, (b) $\bar{E} \in [-0.0024, 0]$ with $\gamma = -1.72 \pm 0.24$, (c) $\bar{E} \in [-0.0571, -0.0548]$ with $\gamma = -0.71 \pm 0.12$, (d) $\bar{E} \in [-0.0015, 0]$ with $\gamma = -1.49 \pm 0.31$, (e) $\bar{E} \in [-1, -0.9985]$ with $\gamma = -0.12 \pm 0.03$, and (f) $\bar{E} \in [-0.1542, -0.1527]$ with $\gamma = -0.58 \pm 0.09$.

can see that we are indeed probing the properties of states with IPR similar to the mean, as the maximum variance across all windows and sizes is ∼5% of the average IPR in that energy window, with the majority being far lower than this. This confirms that we have chosen small enough energy windows and have observed the presence of critical states in the spectra of large systems.

D. Bichromatic potential

The observation of critical states in the 2D GAA model with $\tau_1 = \tau_2$ poses an important question: Are the critical states present a direct result of the weak modulation lines matching the geometry of the tight-binding model (i.e., is the weak modulation along a direction which is connected

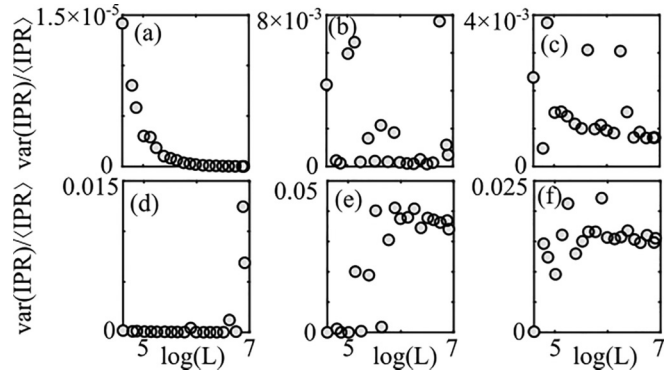

FIG. 8. (a)–(f) Same as Fig. 7 but for the variance of the IPR in each energy window. We plot in each example the variance in the IPR divided by the average IPR in that energy window for each size of the system. The relatively small variance in the IPR confirms that the majority of states within the energy window have an IPR close to the mean.

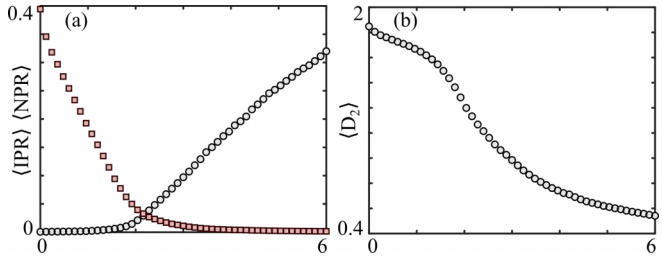

FIG. 9. Mean properties of a bichromatic potential with $\tau_1 = \sqrt{2}$ and $\tau_2 = (1+\sqrt{5})/2$ in the 2D GAA model with deformation $\beta = 0$. (a) The mean over all states of the inverse and normalized participation ratios. (b) The mean over all states of the scaling fractal dimension, D_2.

by tunneling)? As shown in Fig. 1, when $\tau_1 \neq \tau_2$, the weak modulation lines do not follow the geometry of the underlying lattice. We now consider the case of $\tau_1 = \sqrt{2}$ and $\tau_2 = (1+\sqrt{5})/2$ to show that the exact form of the weak modulation lines does not change the presence of critical states. As the 2D GAA potential is now defined by two periods (or frequencies) we will refer to the potential as being bichromatic. We will consider only the case of $\beta = 0$, with nonzero β resulting in similar effects to what has already been observed, e.g., the introduction of mobility edges between extended and localized states and a larger intermediate regime as a result.

We first confirm that the bichromatic potential has an extended-to-localized transition, as shown by the ⟨IPR⟩ and ⟨NPR⟩ in Fig. 9(a). We also see the same behavior as the chromatic case for the mean fractal scaling dimension $\langle D_2 \rangle$ in Fig. 9(b). As shown in Fig. 10(a), there is an extended-to-localized transition of all states with no obvious mobility edge in the spectrum. However, if $\beta \neq 0$, single-particle mobility edges between extended and localized states are still observed. Importantly, we show that the bichromatic potential still supports critical states, as shown by the large region of $0 < \langle D_2 \rangle < 2$ in Fig. 10(b).

IV. ANOMALOUS MOBILITY EDGES AND DIFFUSION

A. Mobility edges

We will now consider in more detail the nature of the mobility edges present and show that there are multiple mobility edges for all spectra of the 2D GAA model. This is due to the presence of anomalous mobility edges between extended or

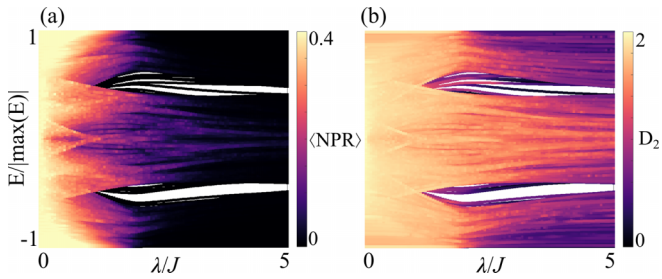

FIG. 10. Properties of a bichromatic potential with $\tau_1 = \sqrt{2}$ and $\tau_2 = (1+\sqrt{5})/2$ in the 2D GAA model with deformation $\beta = 0$. (a) The normalized participation ratios. (b) The scaling fractal dimension, D_2.

localized and critical states in the spectrum, even deep into the extended or localized regime. To see this, we plot the scaling fractal dimension as a function of the eigenenergies for the full spectrum for a number of different values of λ. As a reference point for the influence of the finite size and underlying tight-binding model without a quasicrystalline potential, we plot the case of $\lambda = 0$ in Fig. 11(a). Here we observe that the majority of the states have $D_2 \approx 2$, with deviations being evident for the lowest and highest energy states where the finite size of the system is particularly impactful. There is also a noticeable deviation from $D_2 \approx 2$ at the center of the spectrum; this is due to the properties of states in the central flat band and is typical in 2D noninteracting tight-binding models.

First, we consider the case of equal irrational periods in the 2D GAA potential, with $\tau_1 = \tau_2 = \sqrt{2}$ in Figs. 11(b)–11(e). For $\lambda = J$ as shown in Fig. 11(b), the potential causes the states in the central portion of the spectrum and elsewhere to localize with $D_2 \approx 1$, i.e., their support is effectively that of a one-dimensional system. Therefore for $\lambda < 2J$ there are at least two mobility edges between critical and extended states. Past the localization transition the edges of the spectrum show the presence of localized states with $D_2 \approx 0$, but the central portion of the spectrum remains critical. The complexity of defining mobility edges and when states are extended, critical, or localized becomes evident in Figs. 11(c) and 11(d), as states of similar energy can be characterized by vastly different D_2. It is clear that anomalous mobility edges between localized and critical states will be present and there could even also be some between extended and critical states for modulations close to the critical point, as in Fig. 11(c). When the modulation becomes strong, as is shown in Fig. 11(e) for $\lambda = 10J$, then the majority of states become localized. However, it is clear that a large portion of the states in the central region of the spectrum remain critical and there will still be at least an anomalous mobility edge between localized and critical states. We can confirm that while this central region of critical states does get narrower in energy, it is present even for large modulations up to and including $\lambda = 100J$; see Sec. IV B.

We now consider the case of unequal irrational periods in the 2D GAA potential, with $\tau_1 = \sqrt{2}$ and $\tau_2 = (1+\sqrt{5})/2$ in Figs. 11(f)–11(i). The results are very similar to those of the equal periods already considered, especially for modulation strengths around the transition, as shown in Figs. 11(g) and 11(h). This shows again that the presence of critical states and anomalous mobility edges in the spectrum is not reliant on there being weak modulation lines formed that match the geometry of the tunneling in the tight-binding model. However, the extreme cases of D_2 for both low and high modulation strengths are not present as shown in Figs. 11(f) and 11(i). We also consider the case of fixed $\tau_1 = \sqrt{2}$ with $\tau_2 = \sqrt{3}$ and $\tau_2 = \sqrt{10}$ in Figs. 12(b) and 12(d), respectively. In both cases, we again observe a similar structure in the distribution in D_2 to the cases already discussed in Fig. 11.

We now consider two examples to illustrate the origins of the critical states by having one of the periods be rational. In these examples the model is quasiperiodic only in one direction [that of $(x+y)$ in our case] and periodic or crystalline in the other. We take the case of $\tau_1 = \sqrt{2}$ with $\tau_2 = \sqrt{1}$ and $\tau_2 = \sqrt{9}$ in Figs. 12(a) and 12(c), respectively. We again observe a range of different scaling fractal

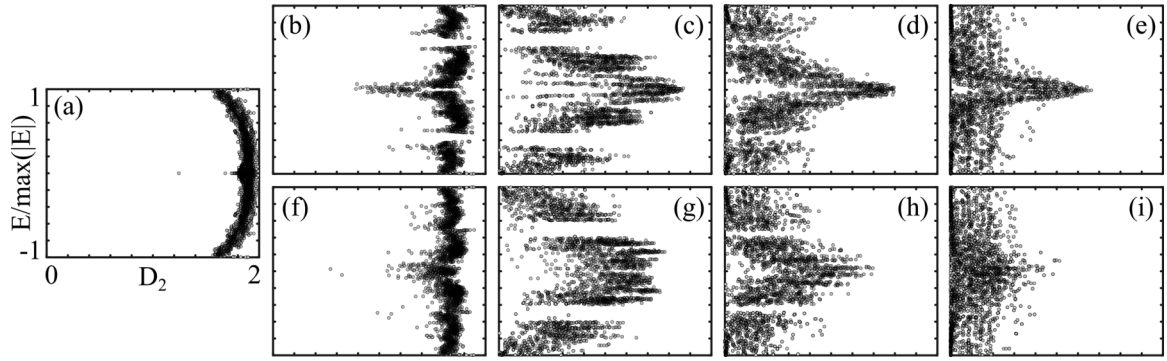

FIG. 11. Examples of the fractal scaling dimension D_2 for each eigenstate of energy E in the 2D GAA model. (a) The trivial case of $\lambda/J = 0$; this gives a reference for the effect of the finite size of the system on D_2. (b)–(e) The case of $\tau_1 = \tau_2 = \sqrt{2}$, and (f)–(i) the case of $\tau_1 = \sqrt{2}$ and $\tau_2 = (1+\sqrt{5})/2$. From left to right are shown increasing modulation strengths of (b) and (f) $\lambda/J = 1$, (c) and (g) $\lambda/J = 3$, (d) and (h) $\lambda/J = 5$, and (e) and (i) $\lambda/J = 10$. For all cases of $\lambda \neq 0$ at this system size the spectrum includes critical states, i.e., $0 < D_2 < 2$, and there are many anomalous mobility edges with no single clear mobility edge.

dimensions for states throughout the spectrum. The origin of the critical states for the superlattice setting is particularly clear in Figs. 12(a) and 12(c) with a large number of states having $D_2 \approx 1$, i.e., they are one-dimensional states, and this is due to the system now being effectively a set of coupled 1D chains of tight-binding models with weak modulation or variation in the disorder in one of the dimensions, as was used to build the 2D AA model from stacking AA chains [51]. Interestingly, we observe similar properties of the states for both $\tau_1 = \tau_2 = \sqrt{2}$ and the bichromatic quasiperiodic case at the same value of $\lambda = 3J$ as shown in Figs. 11(c) and 11(g), respectively.

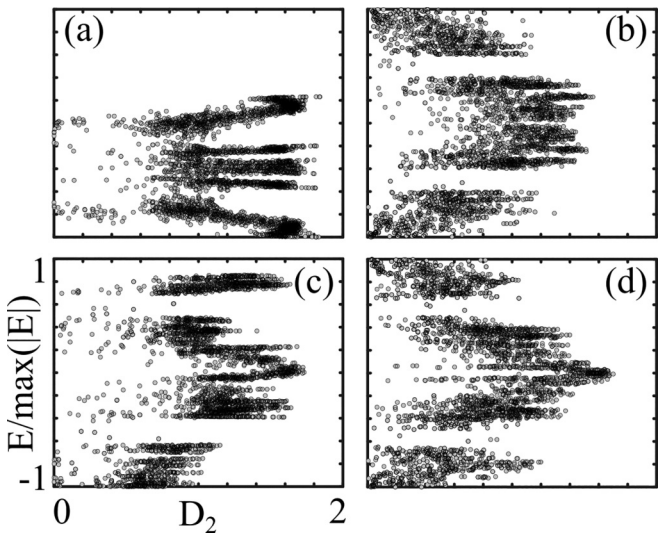

FIG. 12. Examples of the fractal scaling dimension D_2 for each eigenstate of energy E in the 2D GAA model for fixed $\tau_1 = \sqrt{2}$ and $\lambda/J = 3$ with varying τ_2. Shown are examples of (a) $\tau_2 = \sqrt{1}$, (b) $\tau_2 = \sqrt{3}$, (c) $\tau_2 = \sqrt{9}$, and (d) $\sqrt{10}$. The examples in (a) and (c) are therefore crystalline in a single direction as the potential is a set of repeating 1D quasiperiodic chains, and this is reflected in the number of states with $D_2 \approx 1$ shown in each case.

B. Diffusion

We have so far shown that critical states play a central role in the spectral properties of the 2D GAA model and that this results in the presence of many anomalous mobility edges between critical states and localized or extended states in the spectrum. We will now investigate how this impacts the physical properties of the 2D GAA model by considering the diffusion properties of initially localized states. The state will be initialized at a single site, and as the model is quasiperiodic through the on-site potential, this means that starting at different initial sites will be equivalent to starting at different energies. By changing the initial site that is populated we can then sweep through the spectrum, allowing us to probe the impact of the mobility edges present on the diffusion of an initially localized state. The initial state will be propagated under the time-independent Hamiltonian described in Eq. (1) for a fixed total duration of time in the first instance. We will specifically study the same 60×60 system with open boundaries that we have focused on to this point and evolve for a time $t = 100J^{-1}$. In order to measure the diffusion of the particle through the system we will measure the mean-square deviation

$$\sigma_x = \sqrt{\langle x^2 \rangle - \langle x \rangle^2}, \tag{12}$$

where $\langle x \rangle$ is the expectation in x of the state. Note that we will consider the case of $\beta = 0$ in detail and focus on the spread in a single dimension σ_x with similar results observed for σ_y.

In Fig. 13(a) we show the maximum mean-square displacement across λ for states that probe different parts of the spectrum. As expected, we observe that for all parts of the spectrum, the maximum mean-square displacement starts off large for small λ, as the system is fully described by extended states. As λ is tuned to higher values the extent of the state after propagation decreases, with a transition at the AA delocalized-to-localized transition point of $\lambda = 2J$. After this point, the different energy states begin to behave differently. The state initialized close to the ground state energy is converging to a small mean-square deviation, a clear sign that the states around this energy are becoming more and more localized as has been reflected for the ground state in results throughout this paper. However, states initialized

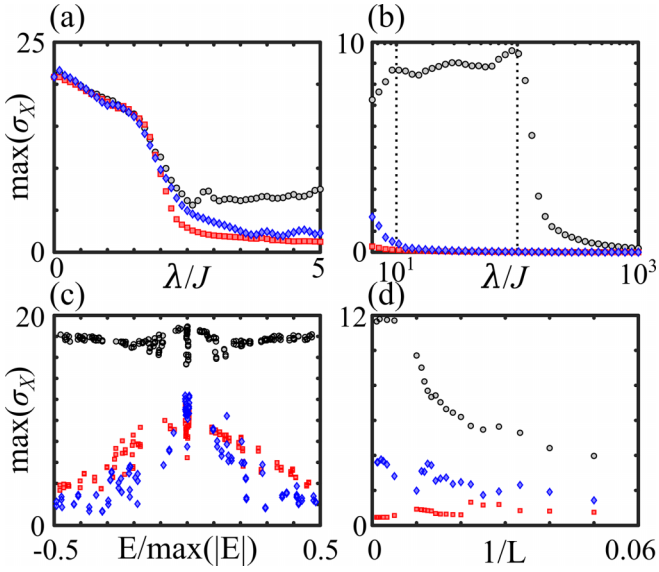

FIG. 13. Anomalous diffusion in the 2D GAA model for $\beta = 0$ and $\tau_1 = \tau_2 = \sqrt{2}$. (a) and (b) The maximum mean-square displacement across potential strengths λ/J after $t = 100J^{-1}$ for states initially localized to a single site. Initial states of different energy are shown, with squares (red) showing a state with energy near the ground state, diamonds (blue) showing a state at approximately half of the ground state, and circles (gray) showing a state with $\bar{E} \approx 0$. (c) The distribution of maximum mean-square displacement at various λ after $t = 100J^{-1}$, with circles (gray) being $\lambda = J$, squares (red) being $\lambda = 3J$, and diamonds (blue) being $\lambda = 5J$. (d) Scaling of the maximum mean-square displacement as a function of the side length L with $\lambda = 4J$ after $t = 100J^{-1}$ and the points as described for (a) and (b).

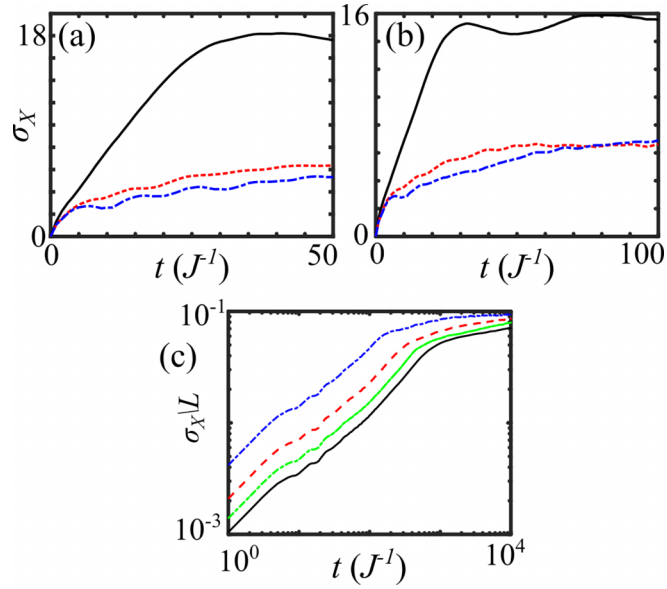

FIG. 14. Expansion of localized states in the 2D GAA model with $\tau_1 = \tau_2 = \sqrt{2}$. The mean-square displacement is shown at each point in time as an initially localized state is propagated in time with the 2D GAA Hamiltonian. (a) and (b) The cases of $\lambda = J$ (solid black curve), $\lambda = 3J$ (dash-dotted blue curve), and $\lambda = 4J$ (dashed red curve) for an initial localized state with $\bar{E} \approx 0$ for $\beta = 0$ (a) and $\beta = 0.3$ (b). (c) The case of $\lambda = 4J$ and $\beta = 0$ for long-time dynamics for large systems of size $L = 250$ (dash-dotted blue curve), $L = 500$ (dashed red curve), $L = 750$ (dash-dotted green curve), and $L = 1000$ (solid black curve).

close to the center of the spectrum at $E \approx 0$ at first follow this trend towards small mean-square displacement but converge to a nonzero value for large λ due to the presence of transport-supporting critical states. States between the ground state and center of the spectrum largely follow the qualitative form of the ground state trend but with a clear extended transition in going to small σ_x due to the presence of critical states.

The middle and $E \approx 0$ states both converge to the small mean-square displacement obtained for the ground state for large λ as shown in Fig. 13(b). How this happens for the $E \approx 0$ states is particularly interesting; the critical states supporting the nonzero mean-square displacement are stable well into large λ. However, this diffusion is eventually destabilized for dominating λ of order $10^2 J$, and then at $10^3 J$ the eigenstates are simply the Hilbert space, i.e., the occupation of each individual site, as the Hamiltonian is effectively only the on-site potential. As the potential takes values throughout the range between $-\lambda$ and λ, the eigenstates will be increasingly zero dimensional, and the starting state will have significant overlap with a single eigenstate resulting in no diffusion as is observed for $\lambda = 10^3 J$.

The exhibited diffusion properties for the states are not unique to the three examples shown in Figs. 13(a) and 13(b), with Fig. 13(c) showing the spread of the maximum mean-square displacement across the range of energies in the central portion of the spectrum for various λ. We also confirm that this is not a finite-size effect by considering the scaling of the maximum mean-square displacement up to $L = 1000$ in Fig. 13(d), with a clear convergence for large systems giving a propagation limit in this fixed total time of propagation. We show an example of the long-time dynamics in Fig. 14(c), showing that for 2D lattices of up to 10^6 sites, critical states can host diffusion of an initially localized state. Note that σ_x/L decreases with increasing system size but that even after $t = 10^3 J^{-1}$, the dynamical state is still slowly diffusing and the maximum σ_x is not yet necessarily reached. Also, the number of possible starting sites for an initially localized particle to have similar energy and hence to reach this maximum σ_x is also increasing.

Finally, we show the mean-square displacement as time evolves for an initial state at $E \approx 0$ and localized to a single site in Fig. 14 for both the case of $\beta = 0$ as discussed so far and the case of $\beta = 0.3$. For zero or nonzero β the displacement for states at small λ, i.e., $\lambda = J$, is shown; there is a clear linear transport regime, reflecting the ballistic expansion of the initially localized state into the space, followed by a saturation as the state has spread through the majority of the lattice. However, if we consider λ across the standard AA localization transition point, where $\lambda = 3J$ and $4J$ are shown, then there is a departure from the ballistic transport in favor of a subdiffusion regime where the particle spreads more slowly through the lattice. To observe this, we consider in Fig. 14(c) the long-time properties of the displacement for large systems of various sizes $L = 250$, 500, 750, and 1000, remembering that the system has $L \times L$ sites, with $\lambda = 4J$. We observe

straight lines on this log-log plot for all sizes confirming that the displacement as a function of time is a power function and that the displacement has different regimes. The power function $\tilde{t}^{\alpha}$, with $\tilde{t} = \log_{10}(t)$, can be fitted for, and we find that in the region $\tilde{t} \in [1.8, 2.8]$, $\alpha = 0.713 \pm 0.002$ for $L = 1000$ and $\alpha = 0.682 \pm 0.004$ for $L = 750$, which is indicative of subdiffusion as $\alpha < 1$. At late times, e.g., $\tilde{t} \in [3, 4]$, we find that $\alpha = 0.120 \pm 0.001$ for $L = 1000$ and $\alpha = 0.137 \pm 0.001$ for $L = 750$, which is subdiffusive and could be consistent with saturation of the displacement as the wave function expands across the full finite system. This reflects the results of Fig. 13 and shows that the nonzero mean-square displacements observed across the central portion of the spectra and for a broad range of λ are impacted by the presence of critical states. We leave a more extensive study of this subdiffusion regime for a later work including the consideration of more values of the quasiperiodic potential strength and the energy of the initial state for systems of large size.

V. CONCLUSIONS

We have investigated the single-particle properties of two-dimensional models with quasicrystalline on-site terms through the 2D GAA model. It has been shown that similar physics to the 1D GAA model can be observed, with there being an intermediate regime and the deformation property of the potential introducing at least one mobility edge between extended and localized states. We have also shown that critical states are a general property of single-particle diagonal quasicrystalline models. This includes the support of critical states within both the localized and extended regimes of the lattice and for a range of deformations β and different combinations of the irrational periods τ. These models also host many anomalous mobility edges in their spectra both between localized and critical states and between extended and critical states, which we have confirmed for systems of size $L = 60$ and through a scaling analysis of the IPR. This especially impacts the transport properties of the microscopic model, with it being possible to observe expansion through the presence of critical states.

There are a number of open questions that arise from this work, with the key one being how the critical states impact the behavior of many-body quasicrystalline models. In particular, how does the presence of critical states impact the formation of phases such as the Bose glass, contribute to glassy dynamics, and alter the prospects of many-body localization? In the latter case, it can be speculated that the critical states would thermalize any localized state in the long-time limit. Initial results have shown promise of a stable many-body localized phase [50], but these are limited by relatively small system sizes for quasicrystalline systems with ∼100 total sites.

With the current difficulty in pursuing full-spectrum results or long-time dynamics in many-body numerical calculations, a route forward could be to study this system in a controlled experimental setting, e.g., with ultracold atoms in optical lattices [64–66]. The 2D quasicrystalline optical potential realized in Ref. [16] will contain critical states, and this has been investigated via numerics at the single-particle level [23,67]. The geometry of the 2D GAA model considered in this paper is a crystalline square lattice which can be realized through the generation of an optical lattice. The on-site modulation can then be realized either by a second rotated and weaker optical lattice or through the manipulation of the individual lattice sites through digital mirror devices or spatial light modulators. The interaction of the atoms can then be controlled through Feshbach resonances and tuning the depth of the confining optical lattice [64–66], allowing for the realization of the Bose-Hubbard model in the 2D GAA model. The interactions can be tuned to zero, and the physics discussed here could be observed. One can then envisage looking at increasing the interactions to attempt to observe the impact of the critical states on both the ground state and transport properties of the many-body system. While currently ambitious, this would be a similar experiment to that recently conducted to observe delocalization mechanisms for 1D disordered systems with a quantum gas microscope [68].

The data for this manuscript is available in open access at [69].

ACKNOWLEDGMENTS

The author thanks D. Johnstone, L. Sanchez-Palencia, E. Gottlob, and A. J. Daley for helpful discussions. The author acknowledges support from EPSRC through Programme Grant DesOEQ, Grant No. EP/P009565/1.

[1] D. Shechtman, I. Blech, D. Gratias, and J. W. Cahn, Phys. Rev. Lett. **53**, 1951 (1984).
[2] T. Janssen, G. Chapuis, and M. De Boissieu, *Aperiodic Crystals: From Modulated Phases to Quasicrystals: Structure and Properties*, 2nd ed. (Oxford University Press, New York, 2018), pp. 305–405.
[3] C. Berger and T. Grenet, in *From Quasicrystals to More Complex Systems*, edited by F. Axel, F. Denoyer, and J. P. Gazeau (Springer-Verlag, Berlin, 2000), pp. 49–83.
[4] G. Roux, T. Barthel, I. P. McCulloch, C. Kollath, U. Schollwöck, and T. Giamarchi, Phys. Rev. A **78**, 023628 (2008).
[5] X. Deng, R. Citro, A. Minguzzi, and E. Orignac, Phys. Rev. A **78**, 013625 (2008).
[6] H. Tsunetsugu, T. Fujiwara, K. Ueda, and T. Tokihiro, Phys. Rev. B **43**, 8879 (1991).
[7] T. Rieth and M. Schreiber, Phys. Rev. B **51**, 15827 (1995).
[8] P. Repetowicz, U. Grimm, and M. Schreiber, Phys. Rev. B **58**, 13482 (1998).
[9] E. de Prunelé, Phys. Rev. B **66**, 094202 (2002).
[10] S. Iyer, V. Oganesyan, G. Refael, and D. A. Huse, Phys. Rev. B **87**, 134202 (2013).
[11] S. Gopalakrishnan, K. Agarwal, E. A. Demler, D. A. Huse, and M. Knap, Phys. Rev. B **93**, 134206 (2016).
[12] K. Agarwal, E. Altman, E. Demler, S. Gopalakrishnan, D. A. Huse, and M. Knap, Ann. Phys. (Berlin) **529**, 1600326 (2017).

[13] E. V. H. Doggen and A. D. Mirlin, Phys. Rev. B **100**, 104203 (2019).
[14] N. Macé, N. Laflorencie, and F. Alet, SciPost Phys. **6**, 050 (2019).
[15] L. Sanchez-Palencia and L. Santos, Phys. Rev. A **72**, 053607 (2005).
[16] K. Viebahn, M. Sbroscia, E. Carter, J.-C. Yu, and U. Schneider, Phys. Rev. Lett. **122**, 110404 (2019).
[17] M. Sbroscia, K. Viebahn, E. Carter, J.-C. Yu, A. Gaunt, and U. Schneider, Phys. Rev. Lett. **125**, 200604 (2020).
[18] J.-C. Yu, S. Bhave, L. Reeve, B. Song, and U. Schneider, arXiv:2303.00737.
[19] D. Johnstone, P. Öhberg, and C. W. Duncan, Phys. Rev. A **100**, 053609 (2019).
[20] R. Ghadimi, T. Sugimoto, and T. Tohyama, Phys. Rev. B **102**, 224201 (2020).
[21] D. Johnstone, P. Öhberg, and C. W. Duncan, J. Phys. A: Math. Theor. **54**, 395001 (2021).
[22] D. Johnstone, P. Öhberg, and C. W. Duncan, J. Phys. B: At. Mol. Opt. Phys. **55**, 125302 (2022).
[23] E. Gottlob and U. Schneider, Phys. Rev. B **107**, 144202 (2023).
[24] R. Gautier, H. Yao, and L. Sanchez-Palencia, Phys. Rev. Lett. **126**, 110401 (2021).
[25] M. Ciardi, T. Macrì, and F. Cinti, Phys. Rev. A **105**, L011301 (2022).
[26] Z. Zhu, H. Yao, and L. Sanchez-Palencia, Phys. Rev. Lett. **130**, 220402 (2023).
[27] P. G. Harper, Proc. Phys. Soc. Sect. A **68**, 874 (1955).
[28] S. Aubry and G. André, Ann. Isr. Phys. Soc. **3**, 18 (1980).
[29] G. Domínguez-Castro and R. Paredes, Eur. J. Phys. **40**, 045403 (2019).
[30] S. Ganeshan, J. H. Pixley, and S. Das Sarma, Phys. Rev. Lett. **114**, 146601 (2015).
[31] F. Liu, S. Ghosh, and Y. D. Chong, Phys. Rev. B **91**, 014108 (2015).
[32] X. Li, S. Ganeshan, J. H. Pixley, and S. Das Sarma, Phys. Rev. Lett. **115**, 186601 (2015).
[33] C. Monthus, Fractals **27**, 1950007 (2019).
[34] X. Li and S. Das Sarma, Phys. Rev. B **101**, 064203 (2020).
[35] Y. He, S. Xia, D. G. Angelakis, D. Song, Z. Chen, and D. Leykam, Phys. Rev. B **106**, 054210 (2022).
[36] M. Gonçalves, B. Amorim, E. Castro, and P. Ribeiro, SciPost Phys. **13**, 046 (2022).
[37] M. Gonçalves, B. Amorim, E. V. Castro, and P. Ribeiro, Phys. Rev. B **108**, L100201 (2023).
[38] F. A. An, K. Padavić, E. J. Meier, S. Hegde, S. Ganeshan, J. H. Pixley, S. Vishveshwara, and B. Gadway, Phys. Rev. Lett. **126**, 040603 (2021).
[39] Y. Wang, J.-H. Zhang, Y. Li, J. Wu, W. Liu, F. Mei, Y. Hu, L. Xiao, J. Ma, C. Chin, and S. Jia, Phys. Rev. Lett. **129**, 103401 (2022).
[40] V. Goblot, A. Štrkalj, N. Pernet, J. L. Lado, C. Dorow, A. Lemaître, L. Le Gratiet, A. Harouri, I. Sagnes, S. Ravets, A. Amo, J. Bloch, and O. Zilberberg, Nat. Phys. **16**, 832 (2020).
[41] B. Grünbaum and G. C. Shephard, *Tilings and Patterns* (Dover, Mineola, NY, 2016), pp. 15–165.
[42] E. Cockayne, in *From Quasicrystals to More Complex Systems*, edited by F. Axel, F. Denoyer, and J. P. Gazeau (Springer-Verlag, Berlin, 2000), pp. 115–143.
[43] M. Baake, in *Quasicrystals: An Introduction to Structure, Physical Properties and Applications*, edited by J.-B. Suck, M. Schreiber, and P. Häussler (Springer-Verlag, Berlin, 2002), pp. 17–48.
[44] U. Grimm and M. Schreiber, in *Quasicrystals: Structure and Physical Properties*, edited by T.-R. Trebin (Wiley-VCH, Weinheim, 2003), pp. 210–235.
[45] N. Macé, A. Jagannathan, P. Kalugin, R. Mosseri, and F. Piéchon, Phys. Rev. B **96**, 045138 (2017).
[46] A. Szabó and U. Schneider, Phys. Rev. B **101**, 014205 (2020).
[47] T. Liu, X. Xia, S. Longhi, and L. Sanchez-Palencia, SciPost Phys. **12**, 027 (2022).
[48] X.-C. Zhou, Y. Wang, T.-F. J. Poon, Q. Zhou, and X.-J. Liu, Phys. Rev. Lett. **131**, 176401 (2023).
[49] M. Gonçalves, B. Amorim, E. Castro, and P. Ribeiro, Phys. Rev. Lett. **131**, 186303 (2023).
[50] A. Štrkalj, E. V. H. Doggen, and C. Castelnovo, Phys. Rev. B **106**, 184209 (2022).
[51] M. Rossignolo and L. Dell'Anna, Phys. Rev. B **99**, 054211 (2019).
[52] T. Liu, H. Guo, Y. Pu, and S. Longhi, Phys. Rev. B **102**, 024205 (2020).
[53] C. Castellani and L. Peliti, J. Phys. A: Math. Gen. **19**, L429 (1986).
[54] M. Holzer, Phys. Rev. B **44**, 2085 (1991).
[55] M. Schreiber and H. Grussbach, Phys. Rev. Lett. **67**, 607 (1991).
[56] L. J. Vasquez, A. Rodriguez, and R. A. Römer, Phys. Rev. B **78**, 195106 (2008).
[57] F. Evers and A. D. Mirlin, Rev. Mod. Phys. **80**, 1355 (2008).
[58] A. Saul, A. Llois, and M. Weissmann, J. Phys. C: Solid State Phys. **21**, 2137 (1988).
[59] H. Hiramoto and M. Kohmoto, Phys. Rev. B **40**, 8225 (1989).
[60] N. Macé, A. Jagannathan, and F. Piéchon, Phys. Rev. B **93**, 205153 (2016).
[61] Y. Wang, X. Xia, L. Zhang, H. Yao, S. Chen, J. You, Q. Zhou, and X.-J. Liu, Phys. Rev. Lett. **125**, 196604 (2020).
[62] T. Rieth and M. Schreiber, J. Phys.: Condens. Matter **10**, 783 (1998).
[63] H. Q. Yuan, U. Grimm, P. Repetowicz, and M. Schreiber, Phys. Rev. B **62**, 15569 (2000).
[64] M. Lewenstein, A. Sanpera, and V. Ahufinger, *Ultracold Atoms in Optical Lattices: Simulating Quantum Many-Body Systems* (Oxford University Press, New York, 2012).
[65] C. Gross and I. Bloch, Science **357**, 995 (2017).
[66] F. Schäfer, T. Fukuhara, S. Sugawa, Y. Takasu, and Y. Takahashi, Nat. Rev. Phys. **2**, 411 (2020).
[67] Z. Zhu, S. Yu, D. Johnstone, and L. Sanchez-Palencia, arXiv:2307.09527.
[68] J. Léonard, S. Kim, M. Rispoli, A. Lukin, R. Schittko, J. Kwan, E. Demler, D. Sels, and M. Greiner, Nat. Phys. **19**, 481 (2023).
[69] https://doi.org/10.15129/d4b11245-7276-4595-ab24-462caf14b2d4.